



# Investigation on Aerodynamic Behaviour of a SUV Car Model with Vortex Generators at Different Yaw Conditions

G. Shankar<sup>†</sup>, G. Devaradjane and S. Sunil

*Department of Automobile Engineering, Madras Institute of Technology Campus, Anna University, Chromepet, Chennai, Tamilnadu, India*

<sup>†</sup>Corresponding Author Email: [shankarg1990@gmail.com](mailto:shankarg1990@gmail.com)

(Received February 2, 2018; accepted July 8, 2018)

## ABSTRACT

The present work discusses the aerodynamic behaviour of a typical SUV car model mounted with three vortex generators (VGs) similar to the shape of a right-angled triangle in four different yaw angle configurations, the results of which have been quantitatively assessed in the sub-sonic wind tunnel and by using realizable ( $k-\epsilon$ ) model. The VG positioned in the middle is kept in the fixed state while the yaw position of VGs on either side has been modified and its significance is presented in this article. The pressure distribution data along the central plane of the car model for all the cases have been obtained by using 32 channel digital pressure scanner that is connected with the pressure tapings prepared in the symmetrical plane of the car model. Simultaneously two separate cantilever type load cell setup is used in this work to measure the magnitude of drag and lift force with measuring sensitivity of about 0.01N. From the experiments, it is determined that the car model with outer VGs heading the rear windshield and central plane possess the maximum drag and lift coefficient reduction rate of about 4.35% and 3.23% respectively compared to car model without VGs. In addition to these findings it is also determined that the vehicle model with VGs positioned perpendicular to the wind stream direction exhibited strong drag magnitude than that of the vehicle without VGs. This increased drag can be utilized for rapid deceleration of vehicle motion (Aerodynamic braking) particularly at the instance of vehicle is running at high speed conditions. The realizable ( $k-\epsilon$ ) model estimated the drag and lift coefficient closer to that of wind tunnel results and exhibited a maximum error deviation of 2.38%. Further, realizable ( $k-\epsilon$ ) model predicted the existence of the magnitude of velocity gradient, intensity of turbulent kinetic energy variation and streamlined pattern of velocity gradient around the vehicle with VGs compared to the case of vehicle model without VGs at its rear end.

**Keywords:** Ahmed model; Computational simulation; Drag coefficient; Electronic controller; Lift coefficient; Vortex generators; Wind tunnel.

## NOMENCLATURE

|            |                                       |        |                                      |
|------------|---------------------------------------|--------|--------------------------------------|
| $A$        | projected frontal area in $m^2$       | $\ell$ | characteristics length of model in m |
| $C_D$      | coefficient of drag force             | $L$    | length of car model in m             |
| $C_L$      | coefficient of lift force             | $m$    | meter                                |
| $C$        | VG yaw angle Configurations           | $m/s$  | meter per second                     |
| $D$        | VG design                             | $N$    | newton                               |
| $F_{Drag}$ | aerodynamic drag force in N           | $s$    | second                               |
| $F_{Lift}$ | aerodynamic lift force in N           | $V$    | wind Velocity in m/s                 |
| $k$        | turbulent kinetic energy in $m^2/s^2$ | $VG$   | vortex generator                     |

## 1. INTRODUCTION

Globally the availability of conventional fuel is nearing towards famine state in an expeditious manner. This has motivated the current research in

the way of improving the fuel economy of the vehicle. The fuel consumption of the vehicle could be trimmed significantly by implementing active/semi-active flow regulating devices instead of using passive airflow modification techniques in

the vehicle body. The reduction of aerodynamic drag and lift force imposes strong influence in cutting down the fuel consumption of the vehicle substantially at its increased speeds since aerodynamic forces are directly proportional to the square of the vehicle speed. Broad studies have been carried out by many researchers in the past years towards the minimization of effects of aerodynamic drag and lift in the passenger car segment, [Aider \*et al.\* \(2010\)](#) performed an empirical study on the modified curve profiled Ahmed body with trapezoidal shaped VGs as an air deflector for various wind speeds. Authors determined that drag reduction of 14% has been observed by adopting the trapezoidal VG's as an aerodynamic add-on device. The reduced drag force would provide considerable beneficial effects in terms of improved fuel economy of the vehicle. [Belomilan \*et al.\* \(2016\)](#) conducted the experimental analysis on Ahmed model having a rear inclination angle of 25° at different yaw angle condition. The Reynolds number for the test ranges between  $3 \times 10^5$  and  $30 \times 10^5$  for their experimental study. It has been concluded that drag coefficient propagated in a linear way with an increase in yaw angle under the condition of fixed Reynolds number. [Birwa \*et al.\* \(2013\)](#) carried out the computational simulation on AUDI A4 sedan car model by varying ground clearance of the vehicle for different wind speeds. It was noticed that the drag coefficient decreases with increase in wind speed and best drag reduction were observed corresponding to the vehicle ground clearance of 101.6 mm among the other cases. [Castro \(2013\)](#) conducted the combined empirical and numerical study using Detached eddy simulation method (DES) with spalarat-almaras turbulence model in the simplified CAD car geometry. As a result, the numerically obtained values were well correlated with the experimental findings by showing the maximum deviation of 13.8% which lies under the permissible error limit. Hence, DES technique would predict the aerodynamic solutions in an effective manner. [Ghazanfari \*et al.\* \(2014\)](#) performed the numerical simulation on braking characteristics of high speed train fitted with three different design of brake panel as an add-on device. The selection of brake panel was carried based on the parameters like materials type, design and placement of panels. Two panels at each position (Type A) showed increased drag coefficient than the single panel at each position (Type B) thus Type A panel was considered as optimum type of design than the other design configuration. [Gillerion \*et al.\* \(2013\)](#) performed experimental research on Ahmed body having a rear slant angle of 35°. The pulsed jet actuator was used as an air flow deflector located on the rear end roof portion of the Ahmed body. A peak drag reduction of 20% was obtained relative to the base model at an instance of actuators were activated at the frequency of 500 Hertz. [Gilimaneau \*et al.\* \(2008\)](#) performed a computational and experimental study on Ahmed body having rear slant angles of 25° and 35° respectively. Authors disclosed that Ahmed body with 35° slant angle evinced better wake flow pattern in the downstream region whereas, the other one does not replicate the

wake pattern closer to the experimental outcome.

[Howell \(2013\)](#) performed an empirical study on simplified car model by varying its rear slant angle and taper length. Authors revealed that effects of drag reduction occurred at moderate slant angles and contrastingly drag was kept on increasing with increase in its rear taper length. [Howell \(2015\)](#) Carried out an experimental analysis on aerodynamic characteristics of various types of car body at different yaw angles. The authors inferred that the change in vehicle yaw angle imposed a substantial impact on aerodynamic side force and lift force acting on the vehicle which are the predominant factors in determining the vehicle stability. [Jianyong \*et al.\* \(2014\)](#) performed combined experimental and numerical simulation on the high speed train installed with airplane wings as an aerodynamic braking device which was actuated by hydraulic system to decelerate the vehicle motion rapidly. The proposed device was intended to perform four core functions namely, general braking, gradual braking, emergency braking and self-inspection. Numerical results revealed that the deceleration rate of about 8 – 60% has been achieved for the case of vehicle critical running speed lies between 250 and 500 km/hr. Authors concluded that this device provided the deceleration rate of 0.8 m/s<sup>2</sup> even at the vehicle speed of 500 km/hr and it can withstand aerodynamic braking load of 50,000N without any drop in its braking performance. [Koitrant \*et al.\* \(2014\)](#) conducted the experimental investigation on aerodynamic models with front and rear wheel moving technique. Authors concluded that all wheels rotating arrangement would provide more precise data than fixed wheel method. The rotating wheel technique was a little bit expensive and cumbersome. Hence, most of the authors have been adopted a rigid wheel method for performing their study instead of spinning wheel method. [Little wood \*et al.\* \(2012\)](#) dealt with experimental examination on drag reduction using the steady blowing jet method in four different configurations without redesigning the exterior profile of the car model. This research pointed out that among a group of four VG configurations only one showed expected best drag reduction characteristics and it was being noticed at the event of peak momentum coefficient. [Markulund \*et al.\* \(2013\)](#) conducted numerical analysis on two car different models viz, sedan and wagon respectively towards the reduction of aerodynamic drag force and its consequent impact by adopting underbody cover and rear end diffuser as a flow modifier into their vehicle models. The best drag reduction rate was obtained to be 8% and 5% for the sedan and wagon models having underbody cover and diffuser respectively when compared to the standard car models. [Mestiri \*et al.\* \(2014\)](#) performed the experimental analysis on Ahmed body having its back slant angle of 25° fitted with continuous blowing technique at the intersection region of the top of the rear window and rear roof of Ahmed body. The reduction in a drag coefficient of 6 to 10.4% and the instance of reduced boundary layer separation has been observed when the continuous blowing system was actuated. [Sadettin Hamut \*et al.\* \(2014\)](#) performed computational simulation and

experimental investigation on a typical race car model adopted with a spoiler at its rear end and the cases were compared with the base model. The drag and lift coefficient has been significantly reduced to 13.8% and 99.7% respectively relative to the model without spoiler at its end. Takami and maekawa (2017) studied about the aerodynamic braking characterises of high speed train adopted with a pair of two drag panel as an aerodynamic add-on device. They claimed that this device is having the ability to minimize the vehicle stopping distance in the event of failure of conventional mechanical braking system being fitted with the vehicle. Further, the optimum angle of attack between these two drag panels was determined as  $75^\circ$  to  $80^\circ$  that showed superior aerodynamic braking performance and better stability in operating these two panels. TienPhuc *et al.* (2016) carried out the computational simulation around the generic formula one car model using three different turbulence models namely RANS method with realizable ( $k-\epsilon$ ), SST ( $k-\omega$ ) and spalart allmaras method by considering Reynolds number as  $14.9 \times 10^6$  to study the existence of vortex region, velocity magnitude and static pressure distribution along the vertical and horizontal plane of car model. Authors disclosed that among three turbulence models, realizable ( $k-\epsilon$ ) method provided consistent numerical data than the other two turbulence models. Tounsi (2016) investigated the aerodynamic behaviour of Ahmed body having a rear taper angle of  $25^\circ$  mounted with piezo-electric actuators at its rear end region. The intensity of wake gets attenuated and the evidence of the development of little swirling motion of air has been observed at the event of piezo-electric actuators were actuated. Tsubokura *et al.* (2009) conducted the aerodynamic analysis on ASMO simplified vehicle model using wind tunnel measurement and RANS numerical method. The outcome of this study revealed that LES technique would provide precious aerodynamic data than the experimental tests and RANS simulation model. Further it has been reported that it is difficult to study the precise flow pattern around any aerodynamic models from the wind tunnel test.

Wood *et al.* (2015) performed an empirical study on a quarter scaled down typical SUV car model in the subsonic wind tunnel by varying its ride height and underfloor roughness. It has been determined that base pressure was significantly influenced by vehicle ride height whereas variation in underfloor roughness bears only a negligible effect on the aerodynamic behaviour of the vehicle.

At present, only a very few number of research work has been carried out and presented in the stream of semi-active and actively controlled airflow modifiers in the segment of passenger cars. An advanced type of semi-actively controlled yaw angle of three number of right angle profiled VGs that could regulate and minimize the aerodynamic coefficients by assuring enhanced flow guidance around the exterior portions of the car model needs to be developed. As an innovative approach the VG yaw angles were modified by transmitting the electrical pulse to the stepper motor, thereby the various yaw

angle configurations could be obtained and its corresponding aerodynamic coefficients was determined without interrupting the wind tunnel operation for purpose of adjusting the VG yaw angles. Based on the previous literature it has been noticed the VGs with fixed yaw angle alone has been investigated and published by several researchers. In lieu of simplifying the experimental complications in studying the various aspects of VGs at any yaw angles, this system would provide the platform for governing the VG yaw angles in an effective manner. The optimal position of VGs in the vehicle body plays a pivotal role in the reduction of aerodynamic forces and its consequent impact at all the vehicle speeds. Hence, it is significant to locate the VGs likely before the flow separation point of the vehicle body. The drag and lift reduction behavior of these VGs being affixed with the vehicle in four yaw angle pattern and it has been assessed quantitatively based on the experimentation in wind tunnel and CFD simulation on the simplified CAD geometry of the car model.

## 2. EXPERIMENTAL ARRANGEMENT

### 2.1 Wind Tunnel and Evaluation of Drag and Lift Coefficients

Empirical tests were performed in an open circuit, low speed, sub-sonic wind tunnel which has a test dimensions of length 2m, height 0.9m and width 0.8m being employed to study the aerodynamic behaviour of the selected SUV car model. The maximum wind velocity and contraction ratio of the tunnel is 55 m/s and 9:1 respectively. The intensity of turbulence and uniformity in flow were not greater than 0.5% and 0.2% respectively. The wind speed inside the tunnel was monitored with the help of pitot tube mounted on the roof of the test section and it is connected to the conventional inclined manometer. The pitot tube was located at a vertical and horizontal distance of 0.5m and 0.25m from the roof and front head of the vehicle model respectively. The aerodynamic drag and lift force exerted on the testing model for different wind speeds were quantified using dual cantilever load cell arrangement mounted on the base of the test section and the entire force measuring system was kept under the raised platform technique of 0.1m high. The load cells are rigidly fixed to the wind tunnel base while the physical model to be tested is firmly clamped on the measuring tip of the load cell arrangement. The schematic representation of wind tunnel with drag and lift force measuring setup using two cantilever load cells is shown in Figure 1.1 Each load cell is connected to a separate electronic digital force indicator to determine the magnitude of aerodynamic drag and lift force acting on the car model for the respective wind speeds. The sensitivity and data sampling rate of the digital force measurement setup is about 0.01N and 10Hz respectively.

The drag and lift coefficient has been determined using the equations (1) and (2) below

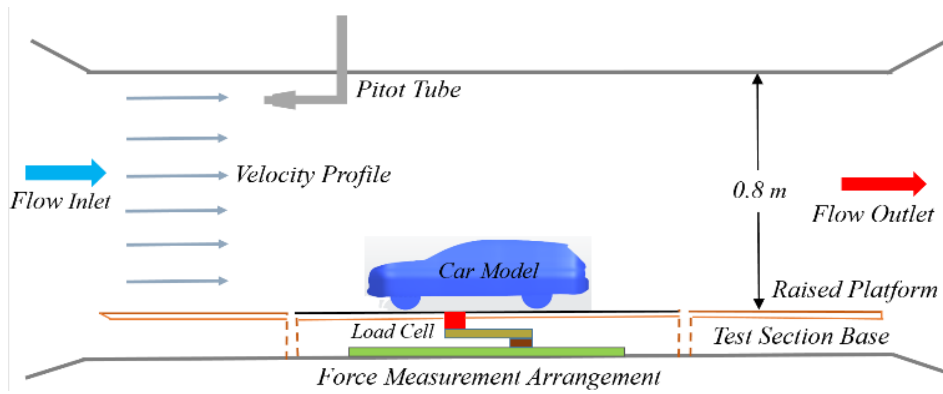


**Fig. 1.1** Layout of open circuit wind tunnel setup.

$$C_D = \frac{2F_D}{\rho \times A \times V_{Wind}^2} \quad (1)$$

$$C_L = \frac{2F_L}{\rho \times A \times V_{Wind}^2} \quad (2)$$

Where,  $C_D$  and  $C_L$  is the coefficient of drag and lift force being measured along and perpendicular to the wind flowing direction.  $A$  is the frontal projected area of the model,  $V_{Wind}$  is the velocity of air flowing inside the wind tunnel and finally  $\rho$  is the density of air in  $kg/m^3$ . The aerodynamic effect of vehicle model at zero yaw angle alone being studied in this work since, it is significant to study the aerodynamic behaviour of vehicle at different yaw angle conditions in order to determine the side and lift characteristics of the vehicle. Only fewer research works have been conducted earlier based on the vehicle at various yaw conditions. However, the study of cross wind behaviour are also much more significant to enhance the vehicle stability.

## 2.2. Testing Vehicle Model

A typical SUV physical car model with VGs at four different yaw angle configurations were being experimentally investigated for its aerodynamic behaviour using a sub-sonic wind tunnel. The vehicle model having its exterior dimensions of 0.433m long, 0.175m wide and 0.140m high being selected and used in the present work. The term blockage ratio is the significant factor to be considered for conducting tests in the wind tunnel (i.e.), the ratio between the projected frontal area of the testing model and cross-sectional area of the inlet duct of the wind tunnel test section being calculated as 2.77%.

The SUV testing car model without and with VGs is depicted in the Figure 1.2 and Figure 1.3 respectively. The flow separation region has been identified and encircled in the Figure 1.4 (Yellow colour) by passing dense white fumes over the testing model using a smoke generator. The boundary layer thickness for the base SUV car model was measured as 25 mm approximately at the rear end roof region of the car model. Koike *et al.* (2004) had suggested that height of VG should be equivalent to the boundary layer thickness, the width of VG should be equals to the one-fourth of the

VG height and length should be twice the height of VG. According to West and Apelt (1982) whenever the calculated blockage ratio is less than 6% the effects of blockage on aerodynamic coefficients and pressure distribution is considered to be negligible and hence, there is no need to include blockage correction factors in determining the equivalent values for the obtained aerodynamic drag, lift and pressure distribution data for the respective vehicle model.

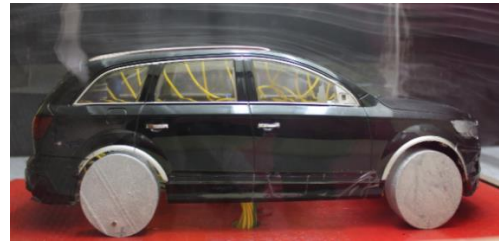


**Fig. 1.2** Base Car model (without VG).



**Fig. 1.3** Car model with right angle design VGs.



**Fig. 1.4** Boundary layer separation zone traced and encircled in the base vehicle model.

The car model without any add-on device is considered as standard or reference model. The drag and lift coefficient of vehicle model with VGs in four yaw arrangement is being compared with the base model and its inferences were presented subsequently in detail.

### 3. DESIGN AND SELECTION OF BEST VG PROFILE

A benchmark and traditional standard road vehicle aerodynamic model known as Ahmed body has been utilized in this work to quantify the effective VG design from the group of five various cross section of VGs. The half scaled down plain Ahmed model having its exterior dimensions of length 0.522m, width and height were generated using typical CAD modeling software and it was further simulated numerically using realizable (k-ε) as a computational tool.

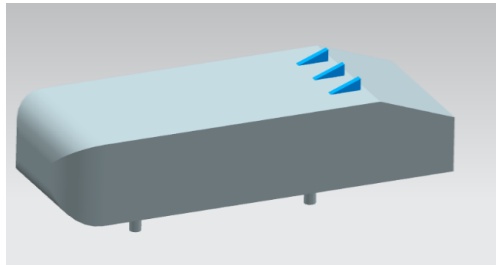


**Fig. 2.1 Ahmed body with right angle triangle VGs at its roof.**

The numerical fluid domain around the Ahmed model is 10L long, 5L wide and 4L high has been generated as an enclosure. Ahmed body with three right triangular VGs at its rear roof is depicted in Figure 2.1 Further the domain has been discretized by prism layered mesh with initial grid height of 0.9 mm, grid height ratio between the successive layers of the grid is 1.2 and the entire domain comprises of  $5.7 \times 10^6$  number of elements approximately used as a reference level of the grid for simulating the Ahmed body along with different VG profiles. The design of VG has been carried out based on the formation of boundary layer thickness which could be measured from the velocity profile of the base Ahmed model. The nomenclature of right triangular profiled VG is shown in Figure 2.2

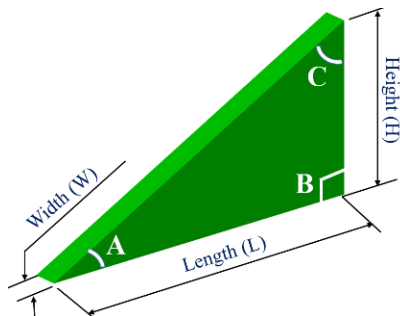


**Fig. 2.2 Nomenclature and interior angular details of right angle triangle profile VG (DN5).**

The interior angular details of the same VG is namely, A, B and C were being measured as 45°, 95° and 45° respectively.

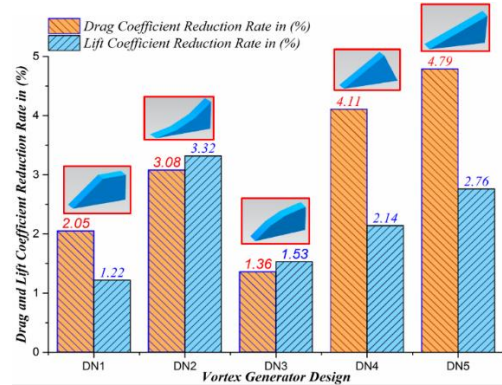


**Fig. 2.3 Drag and lift coefficient reduction rate for Ahmed body with various VG design.**

The thickness of boundary layer for the base Ahmed model was measured as 20 mm approximately at its tail end region. Hence all the five different VG profiles namely, DN1, DN2, DN3, DN4 and DN5 were designed based on the dimensional relation initially proposed by Koike *et al.* (2004).

The DN5 design exhibited the best-attenuated form of kinetic energy distribution than the other VG designs. From the results it has been positively concluded that Ahmed body with DN5 and DN2 profiled VG unveils the best drag and lift coefficient reduction rate of 4.79% and 3.32% respectively related to the model having no VGs at its rear end.

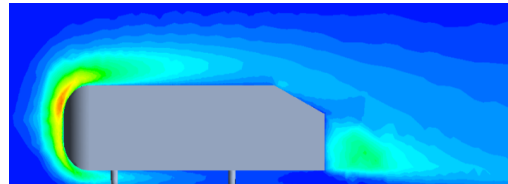


**Fig. 2.4 Turbulent kinetic energy of base Ahmed body.**

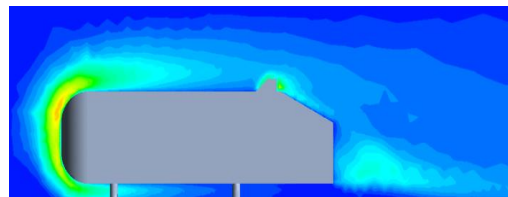


**Fig. 2.5 Turbulent kinetic energy of Ahmed body with DN1 VG design.**

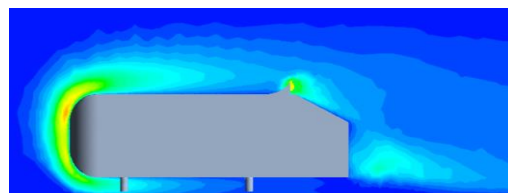


**Fig. 2.6 Turbulent kinetic energy of Ahmed body with DN2 VG design.**

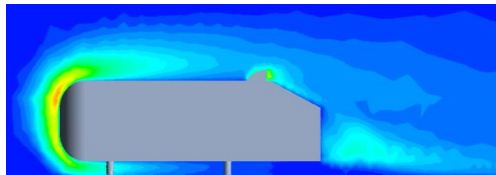


**Fig. 2.7 Turbulent kinetic energy of Ahmed body with DN3 VG design.**

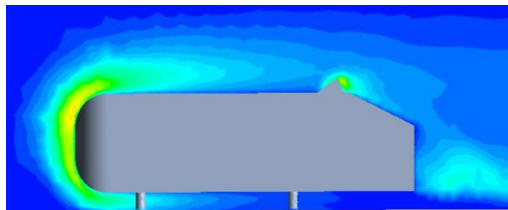


**Fig. 2.8 Turbulent kinetic energy of Ahmed body with DN4 VG design.**

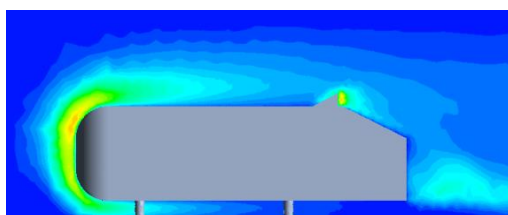
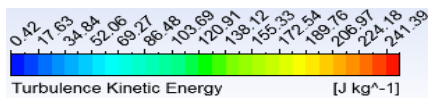


**Fig. 2.9 Turbulent kinetic energy of Ahmed body with DN5 VG design.**



The group of three numbers with five different shapes of individual VG design was being fixed in the rear end roof portion of the standard Ahmed model and further it was computationally analyzed and the outcome of aerodynamic drag and lift coefficient with percentage of reduction rate for the Ahmed model with dissimilar VG profile is depicted in Figure 2.3 The turbulent kinetic energy gradient around the mid-plane of the Ahmed model without and with five different VG patterns is shown in Figure 2.4 and Figure 2.5 – 2.9 respectively. In the present research concern, more preference has been given to the reduction of aerodynamic drag than lift hence, the DN5 VG design would be considered as an effective one for the selected SUV car model and all the wind tunnel tests and numerical simulation have been performed by using this DN5 VG profile and its results were presented successively.

#### 4. ELECTRONIC VG YAW ANGLE CONTROLLER

The dedicated electronic circuit has been designed and utilized in this work for governing the yaw angle of the VGs in precise manner. Among three VGs, the VG placed in the middle is kept in fixed position whereas the yaw of two VGs placed on either side corresponding to central VG has been modified using a stepper motor as an actuator which is having the unit step angle resolution of 1.4°.

$$\text{VG Yaw Angle Position in Degrees} = \frac{\text{No. of Steps Completed by the Stepper} \times \text{Unit Step Angle of the Stepper}}{\text{Unit Step Angle of the Stepper}} \quad (3)$$

The stepper motor was mounted on the underside roof of the car model and VGs are coupled with the stepper armature thereby the angular position of VGs has been altered and its significance were studied. The Arduino uno programmable circuit board is used as a controller to govern the stepper action. The customized program code has been developed and dumped into the arduino controller by means of a computer through connector cable. The push button is provided in the circuit for the purpose of signaling the controller in order to transmit the single electrical pulse to the stepper. The block representation of the VG electronic yaw angle controller is shown in the Figure 2.10. The ratio of number of steps traveled by the stepper and unit step angle gives the total angular degree traveled by the VG from its initial position. The angular position of VG could be calculated by using the equation (3). The number of steps traveled by the stepper can be monitored in the computer connected with the controlling system of the stepper. The electronic unit is designed in such a way that the stepper could be operated in both clockwise and anti-clockwise direction hence, this unit would provide considerable beneficial effects in terms of operating the stepper in an easier way and also it helps in slashing the duration of the empirical tests in the wind tunnel thereby the cost of experimentation could be reduced significantly.

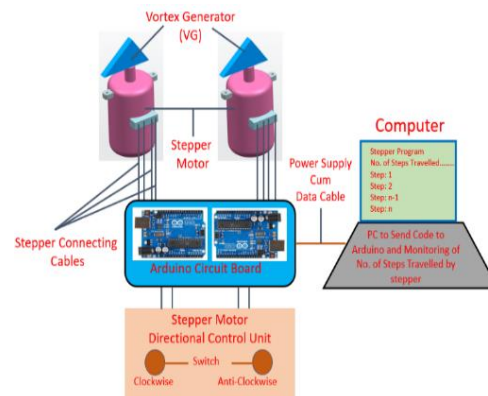


**Fig. 2.10 Block representation of electronic circuit to control VG yaw angle.**

### 5. RESULT DISCUSSIONS

#### 5.1 Pressure Coefficient Distribution

The vehicle model with right triangular profiled VG's in different yaw angle configurations is shown in Figure 3.1 The pressure coefficient distribution over the upper region of the base car model and vehicle with right triangular VG's in different configuration has been studied and reported subsequently. The pressure tapings have been created along the symmetrical plane of the vehicle in order to study the existence of coefficient of pressure distribution pattern for the different cases of VG's

position. The pressure coefficient at every discrete port could be calculated by using the equation (4)

$$C_p = \frac{P_{Port} - P_{Static}}{P_{Dynamic}} \quad (4)$$

$$P_{Dynamic} = \frac{1}{2} \times \rho \times V_{Wind}^2$$

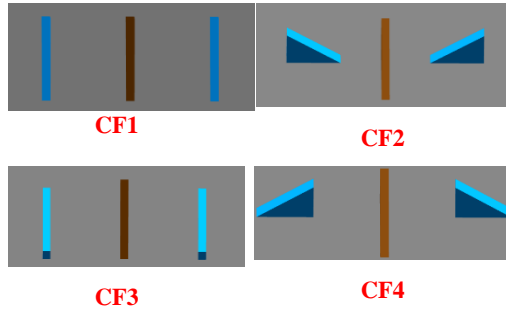


**Fig. 3.1** Different yaw configuration of three VGs.

Where,  $P_{Port}$  is the pressure measured at the individual ports using 32 channel digital pressure scanner,  $P_{Static}$  and  $P_{Dynamic}$  is the static and dynamic pressure measured inside the test section,  $\rho$  is the density of air and finally  $V$  is the wind velocity flowing inside the wind tunnel.

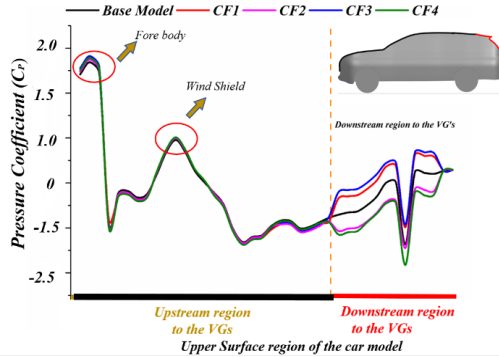


**Fig. 3.2** Pressure coefficient distribution over the upper surface region of the base car model and vehicle with VGs in different yaw conditions.

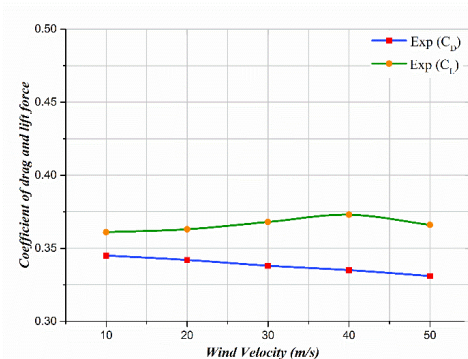


**Fig. 3.3** Drag and lift coefficient of base car model at different wind speeds.

Both static and total pressure could be measured by fixing the Pitot tube facing the wind stream direction. The pressure coefficient distribution plot of the base model and vehicle with VGs in dissimilar configurations for the wind speed of 50 m/s is shown in Figure 3.2. It could be seen that the pressure variation in the upstream region of VGs exhibits small or negligible variation. But contrastingly the  $C_p$  spectrum at downstream to the VGs evinced shift from the  $C_p$  curve of the base model due to an instance of flow gets altered by the VGs and resulting in the formation of turbulent eddies posterior to the vehicle body. The pressure coefficient distribution for vehicle model with VGs in CF2 and CF4 exhibits the trend closer to each other. Both of the above-mentioned cases expelled adverse pressure gradient in the posterior regions of VGs which accelerates the wake formation. The orientation of the two outer VGs in a perpendicular direction to the free stream causes the flow obstruction and leading to increases drag of the vehicle than the base model. In the case of VGs in CF1 and CF3 patterns the existence of reduced pressure gradient has been noticed behind the vehicle compared to the standard model. The above instance takes place due to the placement of VGs in parallel to the direction of the wind and it has the tendency to reduce the early flow separation of air and leading to the formation of attenuated wake region behind the vehicle. Therefore, the reduced drag coefficient has been obtained for the cases of VGs in CF1 and CF3 arrangement when compared to the base model thereby providing least restriction to the forward motion of the vehicle. Comparing all the cases of the vehicle with VG to the base model, it could be concluded that CF3 configuration unveils the least pressure difference between anterior and posterior portions of the vehicle and lead to improvement in fuel economy of the vehicle to some extent.

### Experimental Drag and Lift force

The base car model exhibits similar drag coefficient over the entire range of wind speeds varies from 10 m/s to 50 m/s with the stepping velocity of 10 m/s. The lift coefficient of the testing model was kept on increasing with an increase in wind velocity and gets saturated then steps down at the speed of 50 m/s. The coefficient of drag and lift corresponding to the base car model at 50 m/s were found to be 0.331 and 0.366 respectively. The magnitude of drag and lift force for the same measured velocities is depicted in the Figure 3.3 The Reynolds number for the vehicle model at the wind speed of 50 m/s was calculated as  $1.48 \times 10^6$  based on the length of the car model (0.433m) and the same is mentioned in the equation (5) below

$$R_e = \frac{\rho_{Air} \times V_{Wind} \times l_{Char}}{\mu} \quad (5)$$

Where,  $\rho_{Air}$  is the air density,  $V_{Wind}$  is the velocity of air inside the wind tunnel test section,  $l_{Char}$  is characteristic length of the testing model and  $\mu$  is kinematic viscosity of fluid (Air), Among the four dissimilar VG yaw angle pattern, the effects of drag reduction is highly distinctive when the outer VGs were heading towards aft portion of

the car model (i.e.), CF3 configuration. The variation in reduction rate of aerodynamic drag and lift coefficient for all the four VG configurations relative to the model without VGs are shown in the Figure 3.4. It is clearly observed that the intensity of drag coefficient for the vehicle model with VGs in CF2 and CF4 cases exceed (Marked with negative sign) the drag coefficient of standard car model and the calculated drag coefficient reduction rate for the above two cases were got to be -2.41% and -3.02% respectively compared with the drag coefficient of the base model. The above instance takes place due to the flow obstruction caused by VGs and air gets deflected in the skyward direction leading to an increased wake region behind the vehicle body. As a result, the formation of adverse pressure gradient takes place between the anterior and posterior portions of the vehicle model. Contrastingly the lift coefficient for the VGs in CF2 and CF4 expels the maximum reduction rate of 3.27% and 2.45% relative to the base car model. The orientation of two outer VGs in perpendicular to the wind direction causes the air flow in an upward motion and leading to the increment of negative lift characteristics which enhances the effects of traction and tractive effort of the vehicle. The car model with VGs in CF1 and CF3 pattern unveils better drag reduction behaviour than the other cases since, VGs are positioned along the wind flowing direction and resulting in the formation of turbulent vortices downstream to the VGs. Thus the above instance leading to the formation of the reduced global pressure difference between the front and aft portion of the car model. The flow separation phenomena have been greatly reduced when the VGs were oriented in CF1 and CF3 configurations and causing the attenuated wake region behind the car model and providing improved fuel efficiency characteristics of the vehicle to some extent. From the above discussions it has been disclosed that the vehicle model with VGs in CF3 and CF2 configuration evinces the peak drag and lift coefficient decrement rates of 4.53% and 3.27% respectively compared with the vehicle without VGs.

## 6. NUMERICAL SIMULATION USING CFD

### Numerical Analysis Methodology

The computational analysis on simplified CAD geometry of a car model without and with three right triangular VGs is depicted in the Figure 4.1 and Figure 4.2 respectively identical to the external dimensions of the physical car model being carried out using realizable ( $k-\epsilon$ ) model and it predicted the aerodynamic coefficients closer to the experimental results. Hence, it is decided to adopt the realizable ( $k-\epsilon$ ) model as a simulation code for the entire analysis which could provide the unsteady flow pattern around the car model with sufficient detail. Singh *et al.* (2005) performed the numerical simulation on a truck model to determine the magnitude of boundary layer separation and its effects by applying the above four numerical

models in the CFD-ANSYS GAMBIT application. Authors revealed that realizable ( $k-\epsilon$ ) method evinces better results when compared with the remaining solver models. The two advanced computational simulation methods Viz., Large eddy simulation (LES) and Detached eddy simulation (DES) techniques were available in most of the computational codes. Both LES and DES would highlight the turbulent flow characteristics around the aerodynamic bodies in an excellent manner. The two of the above simulation models requires advanced high configuration computers in order to iterate the complex fluid dynamics equations which directly increases the computation cost. The LES model could predict the formation of large turbulent scales around the flow region but it would provide only less information about turbulent eddies distribution in the vicinity of walls of the system. The DES technique is the hybrid of RANS and LES model which could resolve the limitations of LES method by providing detailed flow pattern around and also the region near to the walls of the system. The computational domain was generated around the car model as an enclosure with its dimensional details being 10L, 5L and 4L corresponding to the longitudinal axis, lateral axis and vertical axis of the car model. The upstream and downstream region was set to the distance of 2L and 7L respectively. All the above dimensions were made relative to the length of the car model (L). No slip boundary condition was applied to the entire surfaces of the fluid domain and wall-bound boundaries of the car model. Uniform flow at the inlet regime of the domain was obtained by assuming the flow condition as zero boundary layer thickness and the intensity of turbulence is not greater than 0.5%. Numerical flow configuration along with coordinate axes of the car model is depicted in the Figure 4.3 and moreover the computation flow physics is assumed closer to the ambience of the empirical testing conditions. The inlet wind velocity of air for the numerical simulation was assumed as 50 m/s and which is relative to the experimental Reynolds number obtained from the wind tunnel tests being carried out earlier and presented. The grid independence tests for prism layered mesh was performed prior to the commencement of entire numerical simulation and its details are illustrated in Table 1. The number of elements, initial grid layer height and grid ratio possesses significant impact in deducing the accuracy of the CFD solution hence, it was studied and tabulated. The entire fluid domain was discretized using prism layered mesh composed of  $6.7 \times 10^6$  number of elements approximately by assuming the initial grid layer distance, and grid height ratio between the successive grid layers was 0.8 and 1.2 respectively. The above-mentioned parameters were considered as the reference level of the grid and it has been used to simulate the base car model and the vehicle with VGs in different configurations. The mesh around the vehicle model was generated using local refinement method and the pictorial representation of numerical grid around the simplified car geometry using prism layered mesh at the central plane of the

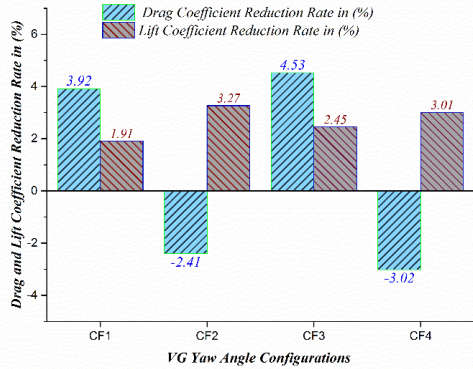


**Fig. 3.4** Drag and lift coefficient reduction rate of vehicle with VGs at various yaw corresponding to the base model.

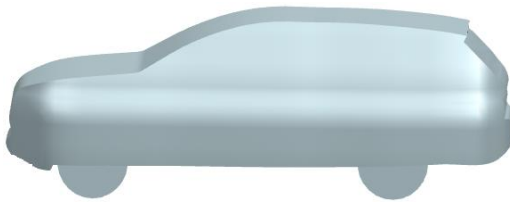


**Fig. 4.1** Simplified CAD geometry of base car model.

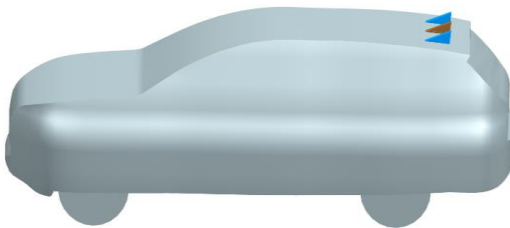


**Fig. 4.2** Vehicle model with three right triangular VGs.

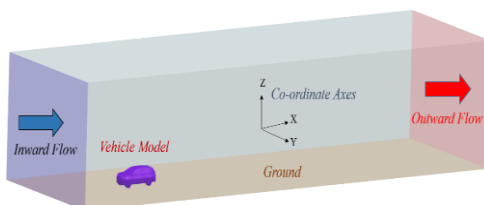


**Fig. 4.3** Computational flow configuration.

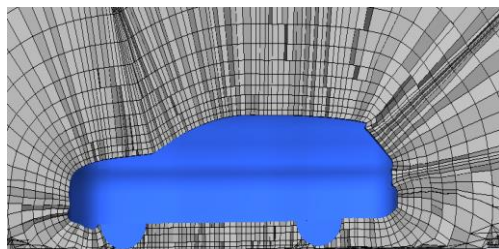


**Fig. 4.4** Prism layered mesh around the symmetrical plane of the vehicle model.

car model with respect to its lateral axis is shown in Figure 4.4. The boundary conditions applied at the different regimes of the numerical domain is illustrated in Table 2. The realizable ( $k-\epsilon$ ) model with SIMPLE (Semi-Implicit Pressure Linked

Equation) algorithm was used as an iterative scheme along with spatial discretization gradient as least square cell-based method has been assumed to simulate all the cases of this research work. The second order upwind scheme was applied for pressure, momentum, turbulent kinetic energy and turbulent dissipation rate for solving the computational solution.

The numerically predicted aerodynamic drag and lift coefficient for the reference car model are 0.325 and 0.359 respectively. The aerodynamic coefficients of drag and lift force for the car model with VGs in four configurations and its reduction rate relative to the base car model are illustrated in Table 3.

The numerically estimated drag and lift coefficients of the car model without and with VGs were slightly underestimates the experimental values. However, the results obtained from the experimental and numerical method were closely correlating with each other showing only a maximum deviation of 2.38% and 2.12% for the drag and lift coefficient respectively. Hence, it is evident that the proposed computational model predicted the solution closer to the results of experimental findings and the deviation between these two methods are depicted in Figure 4.5.

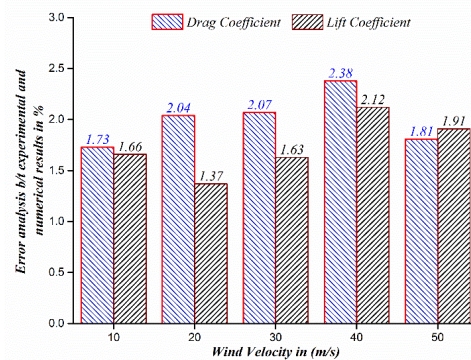


**Fig. 4.5** Error deviation of drag and lift coefficient obtained from empirical and numerical method.

It could be seen that the profile drag is the predominant factor in governing the existence of pressure distribution between anterior and posterior portions of the vehicle model whereas, wall friction drag plays only a negligible role in determining the intensity of aerodynamic forces acting on the vehicle irrespective to its moving velocity. In the current research the magnitude of form drag has been reduced by adopting the three numbers of right triangular shaped VGs placed at the tail end roof portion of the vehicle body where the flow separation takes place in an expeditious manner. From the numerical simulation results, it could be stated that the car model with CF3 and CF2 evinced the best drag and lift coefficient reduction rate of 4.30% and 3.06% respectively compared to the car model without VGs.

### Flow Structures

The existence of flow around the car model without

**Table 1 Grid independence test results**

| Total number of elements in the fluid domain ( $1 \times 10^6$ ) | 1 <sup>st</sup> wall distance in (mm) | Grid spacing ratio | Coefficient of drag ( $C_D$ ) | Coefficient of lift ( $C_L$ ) | Computation duration in (Hours) |
|--|---------------------------------------|--------------------|-------------------------------|-------------------------------|---------------------------------|
| 3.8  | 1.8                                   | 2.5                | 0.339                         | 0.370                         | 6                               |
| 4.6  | 1.5                                   | 1.8                | 0.34                          | 0.366                         | 8                               |
| 5.9  | 1.2                                   | 1.4                | 0.329                         | 0.362                         | 11                              |
| 6.7  | 0.8                                   | 1.2                | 0.325                         | 0.359                         | 13                              |
| 7.6  | 0.6                                   | 1.1                | 0.324                         | 0.357                         | 15                              |

**Table 2 Boundary conditions at all the regions of the fluid domain.**

| Zones           | Boundary Conditions Applied              |
|-----------------|--|
| Inlet           | Velocity ranges b/t (10-50 m/s)          |
| Outlet          | Pressure Reference Gauge Pressure (0 pa) |
| Symmetric Plane | Symmetry                                 |
| Top and Side    | Wall with No-Slip Conditions             |
| Ground          | Wall with No-Slip Conditions             |

**Table 3 Numerical coefficient of drag and lift with reduction rate for various VG configurations.**

| Case Number | Coefficient of drag ( $C_D$ ) | Coefficient of lift ( $C_L$ ) | Reduction rate of drag coefficient in (%) | Reduction rate of lift coefficient in (%) |
|-------------|-------------------------------|-------------------------------|---|---|
| Base        | 0.325                         | 0.359                         | -----                                     | -----                                     |
| CF1         | 0.313                         | 0.353                         | 3.69                                      | 1.67                                      |
| CF2         | 0.332                         | 0.348                         | -2.15                                     | 3.06                                      |
| CF3         | 0.311                         | 0.351                         | 4.30                                      | 2.21                                      |
| CF4         | 0.334                         | 0.349                         | -2.76                                     | 2.78                                      |

and with VGs in different yaw angles have been presented subsequently. Distribution of velocity magnitude and turbulent kinetic energy gradient of the vehicle with VGs from an aerial view is shown in Figure 5.1.

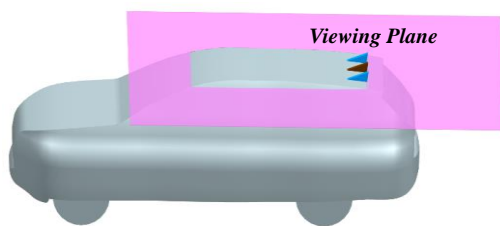


**Fig. 5.1 Imaginary plane (Viewing plane) created at base of the VGs.**

Further, the customized viewing plane has been created and that can be used to reveal the flow pattern at the vicinity of walls around the base car model and vehicle with VGs at dissimilar yaw angle conditions.

**Turbulent Kinetic Energy Distribution**

The study of the formation of turbulent eddies and the magnitude of turbulence could be visualized only with the help of turbulent kinetic energy distribution

plot. Hence the magnitude of turbulent kinetic energy variation for the model with different VG yaw configurations has been presented in this study.

The intensity of turbulent kinetic energy for the reference car model in its roof section is shown in Figure 5.2.

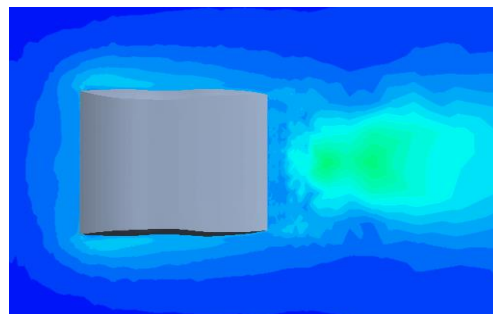


**Fig. 5.2 Turbulent kinetic energy magnitude of base car model.**

The turbulent kinetic energy gradient of the model with VGs in CF2 and CF4 configurations is shown in Figure 5d. and Figure 5f. respectively. The existence of strong magnitude of turbulent kinetic energy gradient could be observed in the downstream

to the VGs. The above instance is mainly due to the orientation of VGs in perpendicular to the wind direction causing rapid flow separation from the vehicle body. The rise in turbulent kinetic energy magnitude causes an increased wake formation and greater adverse pressure gradient was noticed between the front and

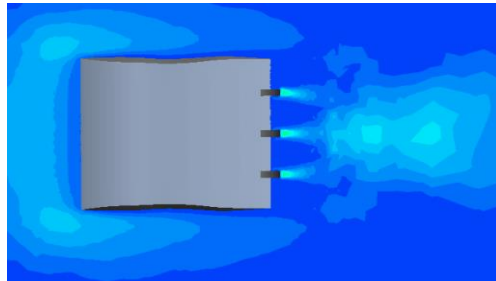


**Fig. 5.3** Turbulent kinetic energy magnitude of vehicle model with VGs in CF1 pattern.

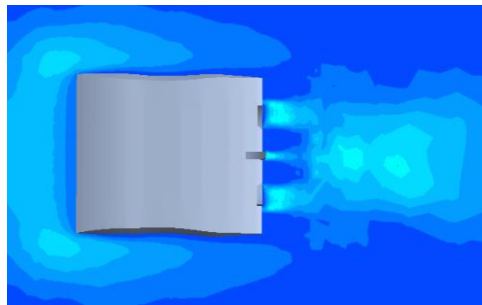


**Fig. 5.4** Turbulent kinetic energy magnitude of vehicle model with VGs in CF2 pattern.

aft portions of the vehicle body. Thus, resulting in restricting the vehicle forward motion which directly affects and trimming the fuel economy of the vehicle. But contrastingly the negative lift characteristics have been improved in the vehicle with VGs in the above two configurations and which provides the additional downforce to the vehicle thereby the tractive effort and traction of the vehicle got improved.

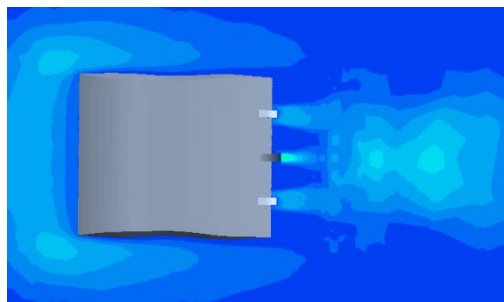


**Fig. 5.5** Turbulent kinetic energy magnitude of vehicle model with VGs in CF3 pattern.

The turbulent kinetic energy variation of the vehicle having VGs in CF1 and CF3 cases is depicted in the Figure 5b. and Figure 5e. and both the cases exhibited an attenuated trend of turbulent kinetic energy gradient behind the VGs when compared with the cases of VGs in CF2 and CF4 configurations.

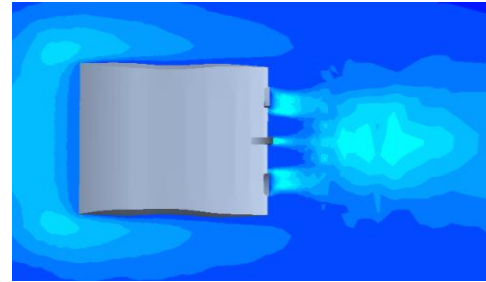
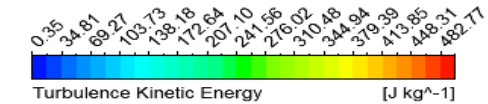


**Fig. 5.6** Turbulent kinetic energy magnitude of vehicle model with VGs in CF4 pattern.



The reduced effect of turbulent kinetic energy in the flow pattern corresponding to the VGs in CF1 and CF3 cases is mainly due to the position of VGs in parallel to the wind flowing direction which enhances the flow attachment with the vehicle body. The attached flow of air with the vehicle results in the reduced pressure difference between front and rear portions of the car body. Even though the cases CF1 and CF3 explore very little variation in exhibiting the attenuated turbulent kinetic energy gradient at the roof plane of the car model, the CF3 pattern expelled the substantial improvement in exhibiting the reduced form of kinetic energy downstream to the VGs than that of remaining cases of VGs configuration. As a result, the reduced effects of aerodynamic coefficients and notable increment in fuel efficiency characteristics of the vehicle could be attained when the VGs are oriented in CF3 configuration.

### Velocity Gradient

It is much more imperative to study the formation of wake or dead water region around the aerodynamic model hence, the pictorial representation of velocity variation at the reference plane of the car model without and with VGs in different configurations has been obtained from the numerical results and presented subsequently. The velocity distribution gradient corresponding to the base car model is illustrated in the Figure 6.1.

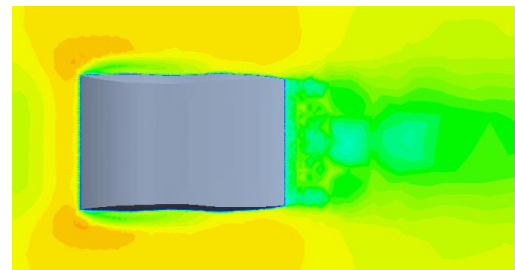


**Fig. 6.1** Magnitude of velocity gradient around the standard car model.

The reduced magnitude of velocity is spotted in the posterior portions of the car body due to the instance of formation of separated flow from the vehicle and resulting in lower velocity distribution past to the vehicle body. Likewise, the velocity distribution of

CF2 and CF4 configuration exhibited the trend closer to the reference model and illustrated in the Figure 6.2 and Figure 6.5 respectively. The magnitude of increased wake region is noticed in the rearward portion of the vehicle with VGs in CF2 and CF4 pattern when compared to the model without VGs. This would lead to increase the adverse pressure difference in the direction of free stream and results in increased drag force. But, contrastingly the reduced sign of lift force has been noticed in both CF2 and CF4 cases because whenever the air stream reaches the front face of the VGs, the air flow got disturbed and deflected in a skyward trend which results in the reduced positive lift of the vehicle and responsible for the improvement of vehicle tractive effort and traction.

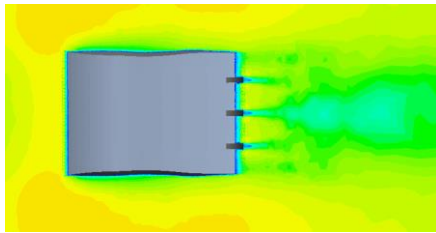


**Fig. 6.2 Velocity gradient around vehicle with VGs in CF1 configuration.**

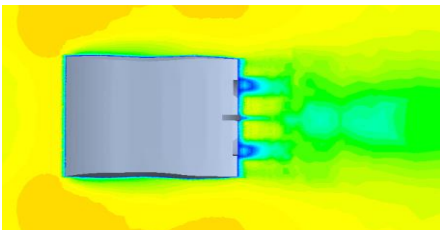


**Fig. 6.3 Velocity gradient around vehicle with VGs in CF2 configuration.**

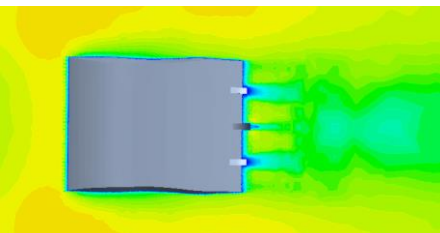


**Fig. 6.4 Velocity gradient around vehicle with VGs in CF3 configuration.**

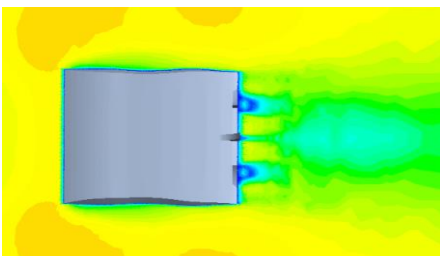
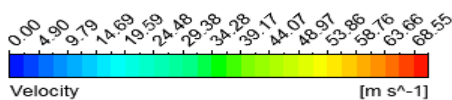


**Fig. 6.5 Velocity gradient around vehicle with VGs in CF4 configuration.**



The pictorial representation of stream wise velocity contour corresponding to the model having CF1 and CF3 cases unveiled the attenuated trend of wake region in posterior portions of the car body and showed in the Figure 6.2 and Figure 6.4 respectively. The above instance is primarily due to the orientation of VGs along the stream wise wind direction and results in guiding the air flow towards wake region of the vehicle body. Consolidating the results of all the cases it has been concluded that the car model with VGs in CF3 configuration highlights the peak depletion of wake region behind the vehicle body than the other three remaining cases and also the vehicle without vortex generators.

**Streamlined Pattern around the Car Model**

The tracing of presence of stream lined pattern around the testing model is a significant task to observe the detailed air flow characteristics (i.e.), flow attachment and detachment points present around the car model in adequate detail.

The existence of velocity streamlines over the base car model is depicted in Figure 7.1. It has been observed that the model without VG showed the separated flow from its exterior profile particularly in the posterior portions of the car model. The flow separation causes larger magnitude of wake region that tends to increased drag acting on the vehicle model.

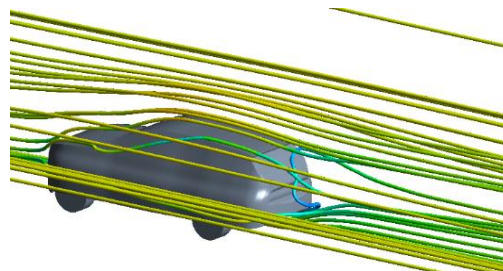


**Fig. 7.1 Streamlined pattern of velocity distribution around the base car model (No VGs).**

The velocity streamlined profiles around the selected car model with VGs in CF2 and CF4 arrangement is shown in Figure 7.3 and 7.5 respectively.

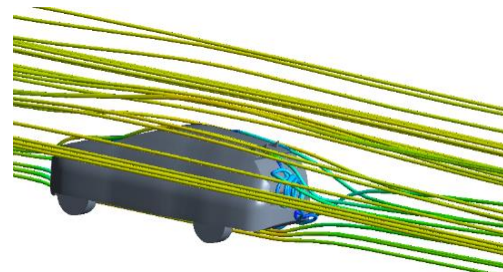


**Fig. 7.2 Streamlined pattern of velocity distribution around the car model with VGs in CF1 yaw arrangement.**

The increased magnitude of flow detachment from the vehicle model has been observed for the model having VGs in these two mentioned (CF2 and CF4)

cases due to the placement of the VGs in perpendicular to wind stream direction.

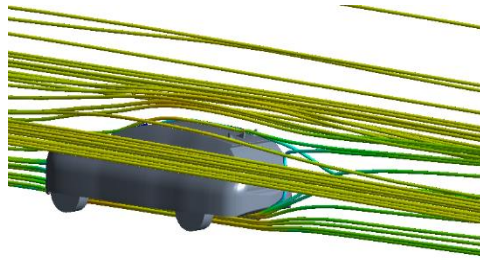


**Fig. 7.3 Streamlined pattern of velocity distribution around the car model with VGs in CF2 yaw organization.**

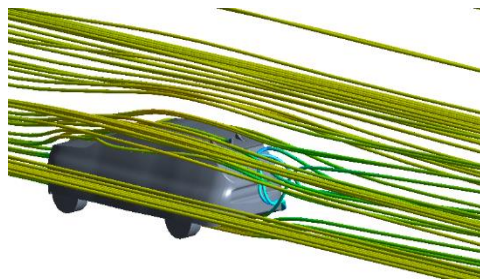


**Fig. 7.4 Streamlined pattern of velocity distribution around the car model with VGs in CF3 yaw configuration.**

The higher wake region tends to resist the vehicle forward motion by forming adverse pressure gradient around the car model and in turn the increased drag value has been noticed for car model attached VGs in these arrangements which may result in increases the fuel vehicle consumption to the great extent.

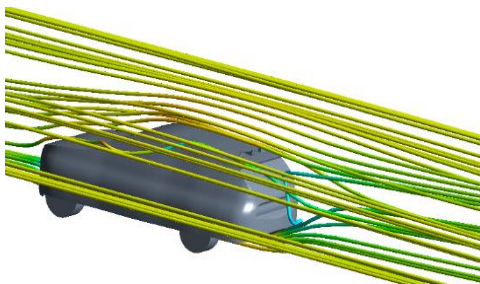
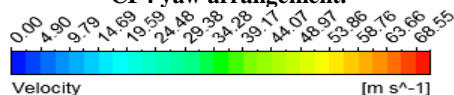


**Fig. 7.5 Streamlined pattern of velocity distribution around the car model with VGs in CF4 yaw arrangement.**



The stream profiles of velocity gradient around the nominated SUV car model with VGs in CF1 and CF3 yaw angle configuration is portrayed in Figure 7.2 and Figure 7.4 respectively.

The presence of attached flow with the car model can be observed post to the placement of VGs over the car model in CF1 and CF3 alignment. The positioning of VGs in parallel configuration

motivates the flow attachment in superior manner that causes reduced magnitude of wake region behind the vehicle body. The car model with VGs in CF1 and CF3 arrangement showed closely similar and better attenuation of wake formation behind the car body it has been observed that the VGs in CF3 configuration exhibited the superior depletion of wake pattern than that of the model with VGs in CF1 arrangement. Further, the reduction in vehicle aerodynamic drag would provide the beneficial effects to the vehicle such as drop in fuel consumption behavior and reduced level of pollutants emitted by the vehicle that can be attained post to the fitment of VGs in CF3 configuration.

## CONCLUSION

This research article reports an extensive study on aerodynamic effects of SUV car model assisted with three numbers of right triangular profiled VGs towards the minimization of drag and lift coefficients are quantitatively assessed by experimenting in the wind tunnel. The peak drag and lift coefficient reduction rate of 4.53% and 3.27% have been observed for a vehicle with VGs in CF3 and CF2 configuration respectively relative to the car model without VGs. It is clearly seen that car model having VGs in CF4 configuration exhibits maximum drag than the other cases and which shows negative implication in the aspect of fuel economy of the vehicle. However, the same increased drag force can be converted into another form of effective and useful work at the instance of braking (Decelerating) the vehicle. This can be achieved by programming the VG yaw control module by commanding the stepper to position the VGs in CF4 pattern at the event of braking alone. This increased drag force offers considerable beneficial effects by providing additional aerodynamic resistance of 10.47 N to the vehicle along with the frictional resistance generated by the vehicle braking system at the speed of 50 m/s. At the instance of vehicle in the normal operating condition, the VGs are allowed to retain its position to CF3 configuration with the help of same VG electronic yaw angle controller unit in order to enhance the aerodynamic property (Anti-drag) of the vehicle. The car model with VGs in CF2 orientation exhibits peak lift coefficient than the remaining cases and results in increased negative lift characteristics thus, providing an improvement in traction and tractive effort of the vehicle. The lift coefficient reduction rate of CF3 patterned VGs unveils the lift coefficient closer to the vehicles with VGs in CF2 and CF4 configurations. From this research it is determined that VGs in CF3 pattern exposed enhanced properties of reduced drag and lift force of the vehicle which results in increased stability by exhibiting least confrontation to the forward motion of the vehicle relative to the vehicle without VGs.

The computational analysis by realizable (k- ε) model predicted the drag and lift reduction characteristics of the vehicle body with triple right-

angle triangle patterned VGs closer to the experimental findings by showing the maximum error deviation of drag and lift coefficient being 2.38% and 2.12% respectively. The realizable ( $k-\epsilon$ ) model suggested that right triangle VG design reduces the influence of aerodynamic drag and lift of the SUV car model through the combined effects of the velocity distribution, magnitude of turbulent kinetic energy distribution and streamlined pattern of velocity gradient between the anterior and posterior portions of the vehicle body.

#### ACKNOWLEDGMENTS

The authors would like to extend their sincere gratitude to Centre for research, Anna University, Chennai, Tamilnadu, India and the committee members of the Anna Centenary Research fellowship (ACRF) for providing their technical and financial assistance throughout this research.

#### REFERENCES

- Aider, J. L., J. F. Beaudoin and J. E. Wesfreid (2010). Drag and lift reduction of a 3D bluff-body using active vortex generators. *Experiments in Fluids* 48(5), 771–789
- Bello-Millan, F. J., T. Makela, L. Parras, C. del Pino and C. Ferrera (2016). Experimental study on Ahmed's body drag coefficient for different yaw angles. *Journal of Wind Engineering and Industrial Aerodynamics* 157, 140–144
- Birwa, S. K., N. Rathi and R. Gupta (2013). Aerodynamic Analysis of Audi A4 Sedan using CFD. *Journal of the Institution of Engineers (India): Series C* 94(2), 105–111
- Castro, N., O. D. Lopez and L. Munoz (2013). Computational Prediction of a Vehicle Aerodynamics Using Detached Eddy Simulation. *SAE Int. J. Passeng. Cars - Mech. Syst.* 6, 414–423
- Ghazanfari, M. and P. Hosseini Tehrani (2014). Study on Braking Panels in High Speed Trains Using CFD. *Advances in Railway Engineering, an International Journal* 2(2), 93-106
- Gillieron, P. and A. Kourta (2013). Aerodynamic drag control by pulsed jets on simplified car geometry. *Experiments in Fluids* 54(2), 1-16
- Guilmineau, E. (2008). Computational study of flow around a simplified car body. *Journal of Wind Engineering and Industrial Aerodynamics* 96, 1207–1217
- Howell, J. (2015). Aerodynamic Drag of Passenger Cars at Yaw. *SAE International Journal of Passenger Cars Mechanical Systems* 8(1), 360-316
- Howell, J., M. Passmore and S. Tuplin (2013). Aerodynamic Drag Reduction on a Simple Car-Like Shape with Rear Upper Body Taper. *SAE International Journal of Passenger Cars - Mechanical Systems* 6(1), 52-60
- Jianyong, Z., W. Mengling, T. Chun, X. Ying, L. Zhuojun and Chen Zhongkai (2014). Aerodynamic braking device for high-speed trains: Design, simulation and experiment. *Proceedings of the Institution of Mechanical Engineers, Part F: Journal of Rail and Rapid Transit* 228(3), 260-270
- Koike, M., T. Nagayoshi and N. Hamamoto (2004). Research on Aerodynamic Drag Reduction by Vortex Generators. *Package Engineering* (2), 11–16
- Koitrand, S., L. Lofdahl, S. Rehnberg and A. Gaylard (2014). A Computational Investigation of Ground Simulation for a Saloon Car. *SAE International Journal of Commercial Vehicles* 7(1), 111-123
- Littlewood, R. P. and M. A. Passmore (2012). Aerodynamic drag reduction of a simplified squareback vehicle using steady blowing. *Experiments in Fluids* 53(2), 519–529
- Marklund, J., L. Lofdahl, H. Danielsson and G. Olsson (2013). Performance of an Automotive Under-Body Diffuser Applied to a Sedan and a Wagon Vehicle. *SAE International Journal of Passenger Cars - Mechanical Systems* 6(1), 2013-01-0952.
- Mestiri, R., A. Ahmed-Bensoltane, L. Keirsbulck, F. Aloui and L. Labraga (2014). Active Flow Control at the Rear End of a Generic Car Model Using Steady Blowing. *Journal of Applied Fluid Mechanics* 7(4), 565-571
- Sadettin Hamut, H., R. Salah El-Emam, M. Aydin and I. Dincer (2014). Effects of rear spoilers on ground vehicle aerodynamic drag. *International Journal of Numerical Methods for Heat & Fluid Flow* 24(3), 627–642
- Singh, S. N., L. Rai, P. Puri and A. Bhatnagar (2005). Effect of moving surface on the aerodynamic drag of road vehicles. *Proceedings of the Institution of Mechanical Engineers* 219(2), 127–134
- Takami, H. and H. Maekawa (2017). Characteristics of a wind-actuated aerodynamic braking device for high-speed trains. In *Journal of Physics: Conference Series IOP Publishing* 822(1), 1-6
- TienPhuc, D., G. ZhengQi and C. Zhen (2016). Numerical Simulation of the Flow Field around Generic Formula One. *Journal of Applied Fluid Mechanics* 9(1), 443-450.
- Tounsi, N., Mestiri, R., Keirsbulck, L., Oualli, H., Hanchi, S., Aloui, F. (2016). Experimental Study of Flow Control on Bluff Body using Piezoelectric Actuators, *Journal of Applied Fluid Mechanics* 9(2), 827–838.
- Tsubokura, M., Kobayashi, T., Nakashima, T., Nouzawa, T., Nakamura, T., Zhang, H., Oshima, N. (2009). Computational visualization of unsteady flow around vehicles using high performance computing. *Computers and Fluids* 38(5), 981–990.

G. Shankar *et al.* / *JAFM*, Vol. 12, No.1, pp. 103-117, 2019.

West, G. S. and C. J. Apelt (1982). The effects of tunnel blockage and aspect ratio on the mean flow past a circular cylinder with Reynolds numbers between  $10^4$  and  $10^5$ . *JAFM*, 3(1), 361-377

Wood, A., M. Passmore, D. Forbes, D. Wood and A. Gaylard (2015). Base Pressure and Flow-Field Measurements on a Generic SUV Model. *SAE International Journal of Passenger Cars - Mechanical Systems*. 8(1), 233-241.